Title: Interfacial energy constraints are sufficient to align cells over large distances

Running title: Energy constraints and cell alignment

S. Tlili[1,2], M. Shagirov[1], S. Zhang[1] and T. E. Saunders[1,3,4,5,#]

[1] Mechanobiology Institute, National University of Singapore, Singapore

[2] Aix-Marseille University, CNRS, UMR 7288, IBDM, Turing Center for Living Systems, Marseille, France

[3] Department of Biological Sciences, National University of Singapore, Singapore

[4] Institute of Molecular and Cell Biology, A*Star, Singapore

[5] Warwick Medical School, University of Warwick, United Kingdom

* Present address:

[#] Correspondence: timothy.saunders@warwick.ac.uk

Abstract

During development and wound healing, cells need to form long-ranged ordered structures to ensure precise formation of organs and repair damage. This requires cells to locate specific partner cells to which to adhere. How such cell matching reliably happens is an open problem, particularly in the presence of biological variability. Here, we use an equilibrium energy model to simulate how cell matching can occur with subcellular precision. A single parameter – encapsulating the competition between selective cell adhesion and cell compressibility – can reproduce experimental observations of cell alignment in the *Drosophila* embryonic heart. This demonstrates that adhesive differences between cells (in the case of the heart, mediated by filopodia interactions) are sufficient to drive cell matching without requiring cell rearrangements. The biophysical model can explain observed matching defects in mutant conditions and when there is significant biological variability. We also demonstrate that a dynamic vertex model gives results consistent with the equilibrium energy model. Overall, this work shows that equilibrium energy considerations are consistent with observed cell matching in cardioblasts, and has potential application to other systems, such as neuron connections and wound repair.

Statement of Significance

Cells often need to identify specific neighboring cells, such as during wound repair and forming neural connections. Here, we develop a biophysical model of such cell-cell interactions within the context of the developing heart. We demonstrate that precise cell matching can occur by minimizing the energy costs of interfacial interactions. This model can explain a breadth of experimental observations despite it being a steady-state approximation of a dynamic system. This opens the possibility that such approaches may be applicable to other systems, providing a powerful yet simple framework for understanding cell matching.

Introduction

During development, cells interact collectively to form tissues and organs through a series of morphological transformations, driven by cell proliferation, rearrangements, migration and death (1-5). When these processes fail, the final shape of the tissue can be defective, resulting in diseases, including cardiomyopathies (6, 7) and neurological defects (8). During organogenesis, cells often need to identify specific cells to which to adhere (9). A classic example is formation of human facial structures (8, 10); cells initially undergo long-ranged migration from distinct regions of the neural plate before forming precise connections to create structures such as the lip. Errors in this process lead to birth defects such as cleft lip and facial cleft (10). During neurogenesis, neurons also need to form precise linkages to their synaptic partners (11-13) with severe consequences if these processes fail. A range of molecules have been identified that are involved in cell matching, predominantly from neuronal systems (14-17). These molecules include cytoskeletal, adhesion, and force transducing proteins (9). However, the underlying mechanisms by which the information from these different components is integrated by the developing tissue to form precise connections remain unknown.

In most tissues, there are multiple cell types with stereotypic spatial positions. For example, formation of the eye requires precise cell fate determination and positioning (18, 19), even within a growing domain (20). In the developing heart, cardioblasts take on different fates depending on expression of (highly conserved) transcription factors (21). Periodic patterns of cells can also be generated from lateral inhibition (22, 23). Such periodic patterns need to be maintained across large distances, even as tissues undergo large-scale morphological changes. Experimental and theoretical work has begun to reveal how neighboring tissues can form distinct boundaries (24, 25). An important concept in generating and maintaining tissue structural organization is the Differential Adhesion Hypothesis (26, 27). By cells mechanically interacting differently with each other, depending on specific fate, cells can form ordered structures and patterns.

Theoretical modelling of tissue formation has helped increase our understanding of how cells pack (28), form compartment boundaries (29), generate complex tissue shapes (30-34), and ensure regulated growth (35). Lateral inhibition can create a wide variety of patterns depending on the feedback mechanisms (36). Recently, vertex models have been used to understand cell

structure in epithelia (37, 38), including in three-dimensions (39). Although biological systems are inherently dynamic, equilibrium statistical mechanics can be a powerful tool for understanding suitable biological processes. An example of such a case is cell packing in the eye, where analogies with soap bubbles provide an effective tool for understanding formation of the *Drosophila* retina (40).

Here, we develop a model of cell matching, where differential adhesion energy constraints between cells drives the process of matching. We apply this to the developing *Drosophila* embryonic heart, where the process of cardioblast cell matching has been quantified (41-43). The *Drosophila* embryonic heart is comprised of two lines of cardioblasts that migrate together over a period of a few hours, Fig. 1A, and they express either Tinman (Tin, the *Drosophila* homolog of mammalian Nkx2.5) or Seven-up (Svp), Fig. 1B, in a repeating 4-2 pattern (44). Cardioblasts first approach each other through migration towards the embryo midline, driven by surrounding tissues (45) and myosin contractility (46), which we refer to as a *ballistic* phase, Fig. 1C. As cardioblasts approach each other, the cells adjust position, via filopodia interactions between cardioblasts, to align accurately with their contralateral partners, Fig. 1D. Specific adhesion molecules are expressed within the different cardioblast types: Fasciclin III (Fas3) in Tin-positive cardioblasts; and Ten-m in Svp-positive cardioblasts, Fig. 1E. Cell matching in the heart depends on the differential spatial expression of these adhesion molecules (41). The mechanical force between opposing cells is generated by a periodic wave of Myosin II in the cardioblasts, that acts to "proof read" the mechanical connections (42, 43). Motivated by these observations, we construct a biophysical model of the cell-cell interactions to test whether such differential adhesion is sufficient to drive cell matching. We then use this model to test how both structural and genetic perturbations alter cell matching. This model provides a biophysical framework in which to understand how cells within confluent tissues find specific partners during development.

Materials and Methods

Methods

Experimental data shown is taken from (41, 42). A detailed methodology for the quantification of heart cell matching is available (43).

Modelling

One-dimensional interface, and mismatch ratio definitions

The model system consists of two rows of equal number of cells interacting on a one-dimensional interface defined as vertices x, Fig. 2A. Each cell i on a row r is represented by a pair of vertices $(x_i^{(r)}, x_{i+1}^{(r)})$ on this interface with $x_i^{(r)} \leq x_{i+1}^{(r)}$ $(\mathrm{i} = 1, 2, \ldots, \mathrm{N}+1$, and $\mathrm{r} \in \{1, 2\}$ for N cells occupying each row), with cell length

$$L_i^{(r)} = x_{i+1}^{(r)} - x_i^{(r)}. \tag{SE1}$$

The total length of a model system is kept constant by fixing first $x_1^{(1)} = x_1^{(2)}$, and last $x_{N+1}^{(1)} = x_{N+1}^{(2)}$ vertices throughout the simulation. The overlap interval length between cells i and j located on two different rows is calculated as:

$$L(i \cap j) = \begin{cases} 0\,, \text{ if } \max\left(x_i^{(1)}, x_j^{(2)}\right) > \min\left(x_{i+1}^{(1)}, x_{j+1}^{(2)}\right) \\ \min\left(x_{i+1}^{(1)}, x_{j+1}^{(2)}\right) - \max\left(x_i^{(1)}, x_j^{(2)}\right), \ \ otherwise. \end{cases} \tag{SE2}$$

The mismatch ratio $m_i^{(r)}$ of a cell i on a row r is defined as a proportion of length of overlap with cells other than its sister cell i', and the total cell length of i:

$$m_i^{(r)} = \frac{L_i^{(r)} - L(i \cap i')}{L_i^{(r)}};\ m_i^{(r)} \in [0,1], \tag{SE3}$$

where the sister cell is defined as a cell i' with same index as i but located on a different row (i.e. $i' = i$), an average mismatch ratio of two sister cells is then calculated as $(m_i^{(1)} + m_{i'}^{(2)})/2$.

Calculating net change in energy

All vertices $x_i^{(r)}$ are assumed to be coupled with harmonic springs, with each cell having an elastic energy $\mathrm{E}_{\mathrm{el,i}}^{(\mathrm{r})} = \mathrm{K} \cdot \left(L_i^{(r)} - \mathrm{L}_{0,\mathrm{i}}^{(\mathrm{r})}\right)^2$, where $\mathrm{L}_{0,\mathrm{i}}^{(\mathrm{r})}$ is the equilibrium length for a given cell (kept constant throughout the simulation), and K is a spring constant. Then, the total elastic energy for the whole system is just a sum of elastic energies over all cells:

$$\mathrm{E}_{\mathrm{el,total}} = \sum_{\mathrm{r}=1}^{2} \sum_{\mathrm{i}=1}^{\mathrm{N}} \mathrm{K} \cdot \left(L_i^{(r)} - \mathrm{L}_{0,\mathrm{i}}^{(\mathrm{r})}\right)^2. \tag{SE4}$$

In the model, two rows of cells interact along the one-dimensional interface by adhesion of cells along segments of the interface shared by the same cell type cells, or by cohesion of cells of two different cell types along interface segments occupied by cells of two different types. We implemented the interface by defining interface vertices $x_j^{(int)}$ with $x_j^{(int)} \leq x_{j+1}^{(int)}$, which could be obtained by concatenating both rows of $x_i^{(r)}$ vertices into single vector and then sorting them. Similar to cell vertices ($x_i^{(r)}$), pair of interface vertices ($x_j^{(int)}, x_{j+1}^{(int)}$) represents an interface segment j. The total adhesion energy for the whole system is then the sum of adhesion energy contributions of all interface segments:

$$E_{adh,total} = \sum_{j=1}^{2N+1} \epsilon_j \cdot (x_{j+1}^{(int)} - x_j^{(int)}) \,, \tag{SE5}$$

where ϵ_j is the cell type specific adhesion energy-per-unit length of a segment j:

$$\epsilon_j = \begin{cases} \epsilon_{aa}, \; j \text{ is interface between type } a \text{ and } a \\ \epsilon_{bb}, \; j \text{ is interface between type } b \text{ and } b \\ \epsilon_{ab}, \; j \text{ is interface between type } a \text{ and } b \end{cases} \tag{SE6}$$

Since vertices of $x_j^{(int)}$ are from both rows of cells, changing position of a single cell vertex $x_i^{(r)}$ could result in cases with $x_j^{(int)} \geq x_{j+1}^{(int)}$, thus $x_j^{(int)}$ needs to be sorted before calculating total adhesion energy during simulation.

The total energy of the system as a function of location of cell vertices $x_i^{(r)}$ is calculated as the sum of elastic and adhesive energies:

$$\mathrm{E}(x) = \mathrm{E}_{\mathrm{el,total}} + E_{adh,total} \tag{SE7}$$

and the net change in total energy due to change in the configuration of $x \rightarrow x + \Delta x$ is calculated as a difference in total energy between the two configurations

$$\Delta \mathrm{E}_{x \rightarrow x+\Delta x} = \mathrm{E}(x + \Delta x) - \mathrm{E}(x) \tag{SE8}$$

Sampling initial configuration and equilibrium lengths of cells

Randomness in cell shape geometry was modelled as a random initial configuration of cells, which was set to be equal to the equilibrium lengths of the cells throughout the simulation. The random initial configuration of cells, and thus the equilibrium lengths ($\mathrm{L}_{0,\mathrm{i}}^{(\mathrm{r})}$) for each cell were sampled from a normal distribution with cell type specific mean and standard deviation using a MATLAB function *normrnd*. In order to construct a random configuration, we implemented random sequential deposition (47) of two rows onto each other with a constraint that enforces equal length of two rows within $\varepsilon = \mu \cdot 10^{-3}$, where μ is the smallest of the two type-specific average lengths of the cells in the given configuration.

For the row of cells with $\mathrm{m_a}$ type a cells and $\mathrm{N} - \mathrm{m_a}$ type b cells, $\mathrm{m_a}$ equilibrium lengths ($\mathrm{L}_{0,\mathrm{i}}^{(1)}$) for the top row are sampled from a normal distribution with mean $L_{0,a}^{mean}$ and standard deviation $L_{0,a}^{std}$, and $\mathrm{N} - \mathrm{m_a}$ equilibrium lengths ($\mathrm{L}_{0,\mathrm{i}}^{(1)}$) are sampled from normal distribution with mean $L_{0,b}^{mean}$ and standard deviation $L_{0,b}^{std}$.

$$\mathrm{L}_{0,\mathrm{i}}^{(1)} \sim \begin{cases} \mathcal{N}\left(\mu = L_{0,a}^{mean}, \sigma = L_{0,a}^{std}\right) \text{ for type a} \\ \mathcal{N}\left(\mu = L_{0,b}^{mean}, \sigma = L_{0,b}^{std}\right) \text{ for type b} \end{cases}$$

where the mean and standard deviation for different cell types are experimentally determined parameters. Next, the bottom row equilibrium lengths ($\mathrm{L}_{0,\mathrm{i}}^{(2)}$) were sampled in the same manner until the constraint $\sum_{\mathrm{i}} \mathrm{L}_{0,\mathrm{i}}^{(1)} - \varepsilon < \sum_{\mathrm{i}} \mathrm{L}_{0,\mathrm{i}}^{(2)} < \sum_{\mathrm{i}} \mathrm{L}_{0,\mathrm{i}}^{(1)} + \varepsilon$ was satisfied. Afterwards, $\mathrm{L}_{0,\mathrm{i}}^{(\mathrm{r})}$ are converted into cell vertices $x_i^{(r)}$ in the same sequence as the $\mathrm{L}_{0,\mathrm{i}}^{(\mathrm{r})}$ was produced by *normrnd* function.

Implementation of Markov-chain cell configuration sampling using Metropolis algorithm

In order to simulate evolution of the cell boundaries by moving cell vertices x and sample cell configurations, we used Monte Carlo Markov-chain (MCMC) sampling by implementing Metropolis algorithm in MATLAB (48). At each MCMC sampling step a vertex $x_i^{(r)}$ is selected randomly and a random move is proposed $x_i^{(r)} \to x_i^{(r)} + \Delta x_i^{(r)}$, $\Delta x_i^{(r)}$ is a Gaussian random variable with mean 0 and standard deviation δX, the value of δX determines magnitude of the random movement (interpreted as random fluctuations in the model). In our implementation $\Delta x_i^{(r)}$ was sampled using *normrnd(0, δX)* function in MATLAB. Afterwards, Metropolis probability of accepting the proposed move, $p(x_i^{(r)} \to x_i^{(r)} + \Delta x_i^{(r)})$ is calculated using

$$p(x_i^{(r)} \to x_i^{(r)} + \Delta x_i^{(r)}) = \min\left(1, exp\left(-\frac{\Delta \mathrm{E}_{x_i^{(r)} \to x_i^{(r)} + \Delta x_i^{(r)}}}{E_0}\right)\right) \quad \text{(SE9)}$$

where $\Delta \mathrm{E}_{x_i^{(r)} \to x_i^{(r)} + \Delta x_i^{(r)}}$ is a net change in total energy of the system due to movement of vertex $x_i^{(r)}$ by amount $\Delta x_i^{(r)}$, and E_0 is the effective temperature ("thermal energy") of the cells. Then, $p(x_i^{(r)} \to x_i^{(r)} + \Delta x_i^{(r)})$ is compared to a uniformly distributed random variable δ_p in the interval $\delta_p \in (0,1)$ produced by *rand* function in MATLAB. If the statement $\delta_p < p\left(x_i^{(r)} \to x_i^{(r)} + \Delta x_i^{(r)}\right)$ is true, then the move is accepted, and otherwise the move is rejected.

Overall, the probability of movement $x_i^{(r)} \rightarrow x_i^{(r)} + \Delta x_i^{(r)}$ of a vertex at position $x_i^{(r)}$ is:

$$P(x_i^{(r)} \rightarrow x_i^{(r)} + \Delta x_i^{(r)}) = \frac{1}{2 \cdot (N-1)} \cdot p(x_i^{(r)} \rightarrow x_i^{(r)} + \Delta x_i^{(r)})$$

where the first term on the right-hand-side refers to the probability of selecting vertex $x_i^{(r)}$ from two rows, and $N-1$ vertices in each row (two end vertices on each row are assumed to be fixed throughout the simulation, and have $P = 0$). In order to avoid flipping of cells, and overlapping of cells on a single row, we forbid such movements by setting $p\left(x_i^{(r)} \rightarrow x_i^{(r)} + \Delta x_i^{(r)}\right) = 0$ for movements with $\Delta x_i^{(r)} > 0$ that exceed cell length of cell i (i.e. $\Delta x_i^{(r)} > 0$ AND $\Delta x_i^{(r)} > L_i^{(r)}$), and for movements with $\Delta x_i^{(r)} < 0$ that exceed cell length of cell $i-1$ (i.e. $\Delta x_i^{(r)} < 0$ AND $|\Delta x_i^{(r)}| > L_{i-1}^{(r)}$).

Implementation of vertex model

Cell initial geometries are constructed using the same functions as with the equilibrium energy model above. Each vertex is described by its position $x_i^{(r)}(t)$,and follows the equation:

$\xi \frac{\partial x_i^{(r)}(t)}{\partial t} = (T_{adh}^{i+1} - T_{adh}^{i} + K * \log(L_{i+1}^{(r)}(t)/L_{i+1,0}^{(r)}) - K * \log(L_i^{(r)}(t)/L_{i,0}^{(r)})$ with $T_{adh} = T_{SS}$ for a S-S interface, $T_{adh} = T_{TT}$ for a T-T interface, and $T_{adh} = T_{ST}$ for a S-T interface. Here, we use the elastic force form $K * \log(L_i^{(r)}(t)/L_{i,0}^{(r)})$ instead of $K * (L_i^{(r)}(t) - L_{i,0}^{(r)})$ to avoid numerical artefacts at big cell deformation. These two definitions are the same for small cell deformations. Time is discretized in time steps dt = 0.01 min and the parameter ξ order of magnitude is tuned to observe the dynamics of the system evolution on the minute/hour timescale. Our previous equilibrium model predicts that matching will occur when $K \backsim T_{adh}$ and on the hour timescale when $T_{adh}/\xi \backsim 1\ \mu m\ /\ min$. In Fig. 6, T_{adh} and K are expressed in pN and ξ in pN *min / μm. The vertices positions are calculated at each simulation step and allow to calculate the mismatch evolution in time.

Results

Mapping of adhesive interactions between filopodia onto an equilibrium energy state

To simulate cell matching, we utilized our energy-based model (Methods) that accounts for the spatial constraints between cells and the adhesion competition between different cell types. In the *Drosophila* heart, differential adhesion between cells is mediated by filopodia contacts, which have a spread of contact times (41, 42), from a few seconds to over five minutes. As justified below, the underlying principle of the model is that these differential filopodia adhesion times between adhering cells can be mapped onto effective adhesion energies.

At a biochemical level, the time for reactions, τ, are typically related to the Arhennius law: $\tau \sim \tau_0 e^{\Delta E/k_B T}$, where ΔE is the energy cost of the reaction. Time scales in biological systems at macroscopic levels often follow the Arhennius law, such as in the developmental time of *Drosophila* embryogenesis (49, 50). Here, we apply a *mesoscopic* approximation, where we assume that the distribution of binding times of filopodia τ_{bind} can be related to the effective adhesion energy barrier ΔE_{adh} to separate contacting filopodia.

In the model, the overlap between facing cells results in an adhesion energy $\Delta E = -\epsilon . x$, where x denotes the length of the cell contact interface and ϵ is the adhesion energy per unit length between the two cells. In previous work (41), we showed that the expression of specific adhesion molecules is patterned along the heart, Fig. 2B; disruption to this pattern leads to matching defects, Fig. 2C. We can encode these adhesion differences as effective energy in our model, Fig. 2D. Cellular compressibility for each cell is encoded by an effective elastic energy $E_{el} = K(L_{cell} - L_0)^2$, corresponding to the cost of deforming the cells away from their preferred cross-sectional width; K is the effective cell compressibility along its leading edge, L_{cell} the cell length and L_0 the cell rest length, Fig. 2D. We only focus on the apical leading edge of the cells as this is where the process of cell alignment is occurring. Combining the energy scales, we can express effective energies for two cell types, denoted by *a* and *b*:

$$E_a = K\left(L_{cell} - L_{0,a}\right)^2 - (\epsilon_{aa}.x + \epsilon_{ab}.y) \quad (1)$$

$$E_b = K\left(L_{cell} - L_{0,b}\right)^2 - (\epsilon_{bb}.x + \epsilon_{ab}.y) \quad (2)$$

ϵ_{ab} denotes the adhesion energy per unit length between cells of type a and b, x and y denote the total alignment overlap with cells of the same and different types respectively, and $L_{0,a}$ and $L_{0,b}$ represent the equilibrium lengths for the different cell types.

Filopodia activity results from the interplay between active fluctuations and adhesion interactions with other filopodia. The active alignment of the heart takes place over a period of around 30 minutes, whereas the average binding time of filopodia is 1-5 minutes. In the following, we assume that the heart has enough time during the active alignment process to reach equilibrium.

To simulate the evolution and equilibration of configurations of heart cell, we use a Metropolis algorithm incorporating mechanical fluctuations induced by filopodia activity as an effective temperature, see Fig. 2E and Methods for further details. We define cellular mismatch by identifying the fraction of cell boundaries that are not correctly aligned with their corresponding opposite cell, Fig. 2A. In this definition, a perfectly aligned tissue has mismatch of 0, while a fully misaligned system has a mismatch of 1. The tissue mismatch is then taken as the average over all cell mismatches.

Minimization of interfacial energy constraints are sufficient to explain cell alignment in the wildtype *Drosophila* heart

We apply our model to the developing *Drosophila* heart, where quantitative data for cell matching is available (41). As well as incorporating the effective energy differences, we need to implement within the simulation a representative pattern of cell types. In the *Drosophila* heart, Tin-positive cardioblasts express Fas3 at high levels and Svp-positive cardioblasts express Ten-m. We translate this into different adhesion energies per unit length between Tin-positive cardioblasts (ϵ_{TT}), Svp-positive cardioblasts (ϵ_{SS}), and between Tin- and Svp-positive cardioblasts (ϵ_{ST}), similar to the outline given in Fig. 1B-E and Fig. 2D.

Initial configuration of the cells and initial cell alignment: By the end of dorsal closure, cardioblasts are brought into close contact. To initiate the cellular arrangement, we assume that the cells at the two ends of the heart are perfectly aligned and are at their resting length initially. To model geometric disorder, we take the length of the apical surfaces for Tin-positive and Svp-positive cardioblasts as $L_{0,T}$ and $L_{0,S}$ respectively. These lengths are simulated as Gaussian variables of mean $L_{0,T}^{mean}$ and $L_{0,S}^{mean}$ with standard deviation $L_{0,T}^{std}$ and $L_{0,S}^{std}$, extracted from

288 experimental quantification of cell size (Fig. 2F). Importantly, the experimentally measured
289 rest lengths are used in the simulations, hence not all cells reach the final size. Given the tissue
290 is constrained *in vivo* (51), these rest lengths represent the balance between the cell intrinsic
291 rest length and external compression. We construct the simulated heart as two rows of cells
292 formed by a succession of four Tin-positive cells and two Svp-positive cells patterns, with a
293 total number of N_1 =52 cells (number of cells in a heart row, Fig. 1B and 2G). Each cell length
294 is picked as a random variable according to the rest lengths distributions (Fig. 2F). However,
295 we constrain the total lengths of the two rows to be identical (Methods).
296
297 *Initial cell matching without adhesion energy:* We first consider the question: are the boundary
298 constraints alone sufficient to ensure robust cell matching? To answer this, we take initial
299 conditions that mirror experimentally measured cardioblast size and position (Fig. 2F-G) but
300 with no adhesion energy (*i.e.* $\epsilon_{TT} = \epsilon_{SS} = \epsilon_{ST} = 0$), Fig. 2D. As we take cells at their initial
301 rest length, no equilibration is needed, and we calculate the mismatch of the initial condition.
302 We performed 30 simulations per condition with confinement of different sizes and calculated
303 the ensemble mismatch in cell alignment. This resulted in a mismatch increasing with system
304 size, Fig. 2H. Interestingly, we find that at 52 cell length (the experimental size of the heart)
305 we get a mismatch around 0.3, which corresponds to the mismatch value experimentally
306 observed in the *Svp*$^{-/-}$ mutants where all cells are of the same type, Fig. 2C. In summary,
307 geometric disorder, induced by cell size variability, is too large to enable precise cell matching
308 merely by boundary constraints.
309
310 *Calculating the mismatch with differential cell adhesion:* We next investigated how the
311 strength of selective adhesion impacts alignment. We first explored matching variations with
312 only one cell type adhering, *i.e.* we varied ϵ_{SS} alone with $\epsilon_{TT} = 0$ $\epsilon_{ST} = 0$, Fig. 3A-C. We
313 computed mismatch evolution as a function of simulation iterations and took its value once it
314 reached a steady-state value, Fig. 3C. The mismatch for each simulation was then averaged
315 over 30 simulations to get the average final mismatch per condition. We find that the final
316 mismatch decreases with increasing adhesion level.
317
318 We then explored two cell types with selective adhesion by using different combinations of ϵ_{SS}
319 and ϵ_{TT} with $\epsilon_{ST} = 0$, Fig. 3D. In general, increased adhesion energy led to reduced mismatch.
320 Different combinations of ϵ_{SS} and ϵ_{TT} can lead to the same alignment. By systematically

varying ϵ_{SS}, ϵ_{TT} and ϵ_{ST}, we see that the equilibrium mismatch is determined by the parameter

$$\gamma = \frac{(\epsilon_{TT}-\epsilon_{ST})+(\epsilon_{SS}-\epsilon_{ST})}{K}, \quad (3)$$

representing the competition between cells due to differential adhesion and cell compressibility, Fig. 3E. Here, γ corresponds to the typical length change that adhesion differences can generate for a single cell. For $\gamma = 0\mu m$, there is no energy cost for different cell types to have a contact interface. The mismatch corresponds to the random case simulated in Fig. 2H; similar to the *Svp*$^{-/-}$ mutant, where all cells are of the same type. Mismatch decreases with increasing γ, reaching a plateau around mismatch of ~ 0.07, dashed line in Fig. 3E. This implies that, beyond a certain level, increasing differential adhesion only weakly improves matching.

We measured spatial variations of the mismatch for different values of γ, Fig. 3F. We find that the mismatch is minimal at the Tin-Svp interface, as any contact between different cell types has some adhesion energy cost for $\gamma > 0\mu m$, Fig. 3G. Alignment of cells inside a block of homogeneous cell types in the high γ limit is determined by the boundaries imposed by the highly aligned cells at the interface between different cell types. Within a region of Tin-positive cells, the level of cell mismatch converges towards the non-adhesive random case with N = 4, Fig. 3H. The mismatch between Svp-positive cells is similar to the random adhesion case with N = 2. The geometric variability in the lengths of the cell leading edges means that cells never reach zero mismatch even at very high adhesion values. Interestingly, for small values of γ, the pattern of cell mismatch is inverted, as geometric variability is higher for Svp cells.

Comparing the spatial profile of cell matching to the experimental data, we see that for $\gamma > 0.5\mu m$ the mismatch profile agrees well with experiment, Fig. 3G. Therefore, simple energy considerations, with a single fitting parameter γ, are sufficient to reproduce the wildtype matching phenotype.

Energy scales are just sufficient to ensure robust matching

We do not know the specific effective energy levels associated with different adhesion interactions. To relate the values of $\epsilon_{TT}, \epsilon_{SS}$ and ϵ_{ST} to the underlying dynamics, we assume that they linearly depend on the energy scales of homophilic interactions of Fas3 (ϵ_{aa}^{Fas3}) and Ten-m (ϵ_{aa}^{Ten}), *e.g.* $\epsilon_{TT} \approx \epsilon_{TT}^{Fas3} + \epsilon_{TT}^{Ten}$. In our model, if there is no differential expression pattern of Fas3 and Ten-m then γ=0 μm; *i.e.* there is no effective adhesion energy differences

354 between cells. For *svp*$^{-/-}$ mutants (where all cardioblasts are Tin-positive) or the double mutant
355 *Fas3*$^{-/-}$; *Ten-m*$^{-/-}$ (Fig. 4A) we expect $\gamma \approx 0$.
356
357 From previous work, the mismatch in a range of mutant conditions – such as disruption of Fas3
358 and Ten-m - is quantified (41). We utilized the results from Fig. 3E to estimate γ for wild-type
359 and mutant conditions (Fig. 4B). We subsequently plotted the mismatch based on the inferred
360 value of γ in a range of conditions (Fig. 4C). Can our model explain the observed values for γ
361 in the mutant conditions?
362
363 From Fig. 4C, we have for the wildtype, $\gamma_{WT} \sim 0.5\ \mu m$, which is smaller than the value $\gamma_{WT} \sim$
364 $1.0\ \mu m$ found by fitting the experimentally measured spatial variation of mismatch (Fig. 3G).
365 However, this difference could be explained by the shallowness of the mismatch curve for γ >
366 $0.5\ \mu m$. Assuming that there is no interaction between Fas3 and Ten-m, we expect that $\gamma_{WT} =$
367 $\gamma_{Fas3} + \gamma_{Tenm}$. We use the measured matching in *Fas3*$^{-/-}$ and *Ten-m*$^{-/-}$ mutants to estimate the
368 contributions to γ_{Tenm} and γ_{Fas3} respectively. From this, we find that $\gamma_{Fas3} + \gamma_{Tenm} \sim \gamma_{WT}$
369 ~0.5 (Fig. 4C).
370
371 To further test these assumptions, we considered additional mutant conditions. Overexpression
372 of Fas3 in Svp cells should give similar value of γ to the *Fas3*$^{-/-}$ mutant, as in both cases the
373 differential expression pattern of Fas3 is largely lost (Fig. 4B). As shown in Fig. 4C this is
374 indeed the case. If Fas3 is reduced in Svp-positive cells, we expect ϵ_{SS} is reduced compared to
375 wildtype. However, ϵ_{ST} is also likely decreased as direct interactions between filopodia with
376 Fas3 is reduced between different cell types. Therefore, we do not expect γ to differ
377 significantly from wildtype. Consistent with this, we find a γ similar to the wild-type case
378 showing that ϵ_{ST} is small compared to ϵ_{SS} and ϵ_{TT}. We can map a range of observations in
379 mutant embryos onto a single curved for the mismatch described by γ, suggesting our adhesion
380 hypothesis is a reasonable approximation of the underlying dynamics driving cell matching.
381
382 **Robustness of cell matching to perturbations**
383 Here, we probe the robustness of the system to perturbations in cell number by considering
384 variations in cell type specification. Within wildtype embryo populations, we observe
385 variability in the spatial pattern of cardioblast specification. For example, we have observed
386 embryos with three and five Tin-positive cardioblasts in a sector, as well as a solitary Svp-

positive cardioblast, and an additional one (Fig. 5). Even when cell number is perturbed, we observe that the boundaries between different cell types are typically well defined. To test the model, we implemented different initial patterns of cardioblasts but otherwise kept parameters identical to the wildtype scenario with $\gamma = 0.5$. The system equilibrates to a state with clear boundaries between the different cell types and cells deform to align boundaries. This demonstrates that having two complementary adhesion processes is robust to perturbations in the structure of the heart as it develops.

Dynamic vertex model of cell matching

To evaluate how differential adhesion modulates cell matching dynamics, we used a vertex approach to model the time evolution of vertices at the interface between the two facing rows of cells, Fig. 6A (see Methods). By analogy with the equilibrium energy model used previously, vertices are submitted to elastic forces corresponding to effective elasticity and adhesion forces in the cell. We assume that adhesion produces a negative tension, which extends cell-cell contact interfaces. The sum of these contributions results in a force which, when divided by an effective friction coefficient, gives the vertex velocity. We explore the simple case of equal tensions, $T_{\mathrm{SS}} = T_{\mathrm{TT}} = -t_0$ and $T_{\mathrm{ST}} = 0$ with a fixed K and friction coefficient, ξ. Varying t_0, keeping other parameters fixed, shows a lower limit to cell matching accuracy, as the time evolution of cell matching collapses onto a single curve for large t_0, Fig. 6B. This limit is consistent with our equilibrium model. At high adhesion differences, the cell mismatch first undergoes a rapid decrease, which is adhesion-dependent. This corresponds to the phase of heterogeneous cell types boundaries shrinking. Below a mismatch of ~0.2, the boundaries between cell types are perfectly aligned, Fig. 6C. The mismatch between cells of the same type decreases with slower, adhesion independent, dynamics that are friction dependent, Fig. 6D. Overall, we see that dynamically incorporating differential adhesion gives similar results to our equilibrium approach, supporting our above assumptions.

Discussion

Even though biological systems are inherently out-of-equilibrium, we have demonstrated that an equilibrium energy argument is consistent with experimental observation of cell matching in the heart. This is consistent with the rapid dynamics of filopodia compared to the time of heart cells final alignment. The filopodia dynamics relate to the system effective temperature. The idea of effective temperatures in developing systems has also recently been used to

describe jamming transitions during zebrafish development (52, 53). Our model shows that cell matching results from the interplay between cell-cell interactions (mediated by filopodia and specific adhesion molecules) and cell deformability. According to our model, the level of differential adhesion found in the wildtype heart is close to the minimal level required to obtain a well-aligned heart as the value $\gamma = 0.5\mu m$ corresponds to the point where the mismatch curve in function of γ starts to flatten. We find that Fas3 and Ten-m contribute almost equally to the matching process. Furthermore, we demonstrate than increasing differential adhesion indefinitely does not accelerate the matching process beyond a certain point as the final alignment phase is adhesion independent.

A key result of our model is that short-ranged constraints (*i.e.* adhesion differences between two cell types) can propagate long-ranged order. We show that generating periodic segments of different adhesion molecules (i) aligns these segments at their interfaces and (ii) alignment inside each segment is due to geometric confinement and decreases with the segment size. Most previous theoretical work on the role of differential adhesion in tissue shaping has focused on how two (or more) distinct tissues can define clear boundaries (25). Our results are complementary to such work, and demonstrate that differential adhesion is a viable mechanism for aligning cells within a single tissue. Recent work has also highlighted how morphogen patterning of tissues coupled with mechanical feedback can build long-ranged tissue architecture (54). It will be interesting to explore how spatial information and mechanical feedback interplay in different tissues to ensure tight domain formation.

Here, we have not considered long-ranged actin structures that span multiple cells. These have been observed during heart closure, and appear to play an important role in cardioblast migration (46). Such structures could also play an important role in integrating mechanical information during closure.

Our work has potential application to other biological systems. During neurogenesis - where precise connections between neurons are required - Notch signaling (involve in lateral inhibition) has recently been shown to regulate neuronal wiring(13). Formation of the vasculature requires cell migration to precise locations and this is mediated by filopodia protrusions and lateral inhibition (55). During wound healing, cells need to repair wounds by forming precise connections. However, how processes at a single cell level are integrated to

ensure long-ranged precise cell matching remains an open question (56). In our model, we do not consider heterogeneities in the mechanical properties. In other systems such as the brain, tuning of tissue stiffness ensures precise cell matching (57). More generally, coordinated cell migration can be directed by tissue stiffening (58). It would be possible to test the role of mechanical feedback in our model by adding viscoelastic relaxation of the cell lengths within a vertex model framework as described in Fig. 6.

Author Contributions

S.T. and T.E.S. designed the project with input from S.Z. S.T. and M.S. performed the simulations and modelling. S.Z. provided all experimental data. S.T. and T.E.S. wrote the manuscript, with contributions from M.S. and S.Z..

Acknowledgements

This work was supported by the University of Warwick, EMBO Global Investigator, Singapore Ministry of Education Academic Research Fund Tier 2 grant (MOE2018-T2-2-135), Singapore National Research Foundation Fellowship (NRF2012NRF-NRFF001-094) and HFSP Young Investigator Grant (RGY0083/2016), all awarded to TES. Tinman antibody was a gift from Manfred Frasch.

Figures and Figure Legends

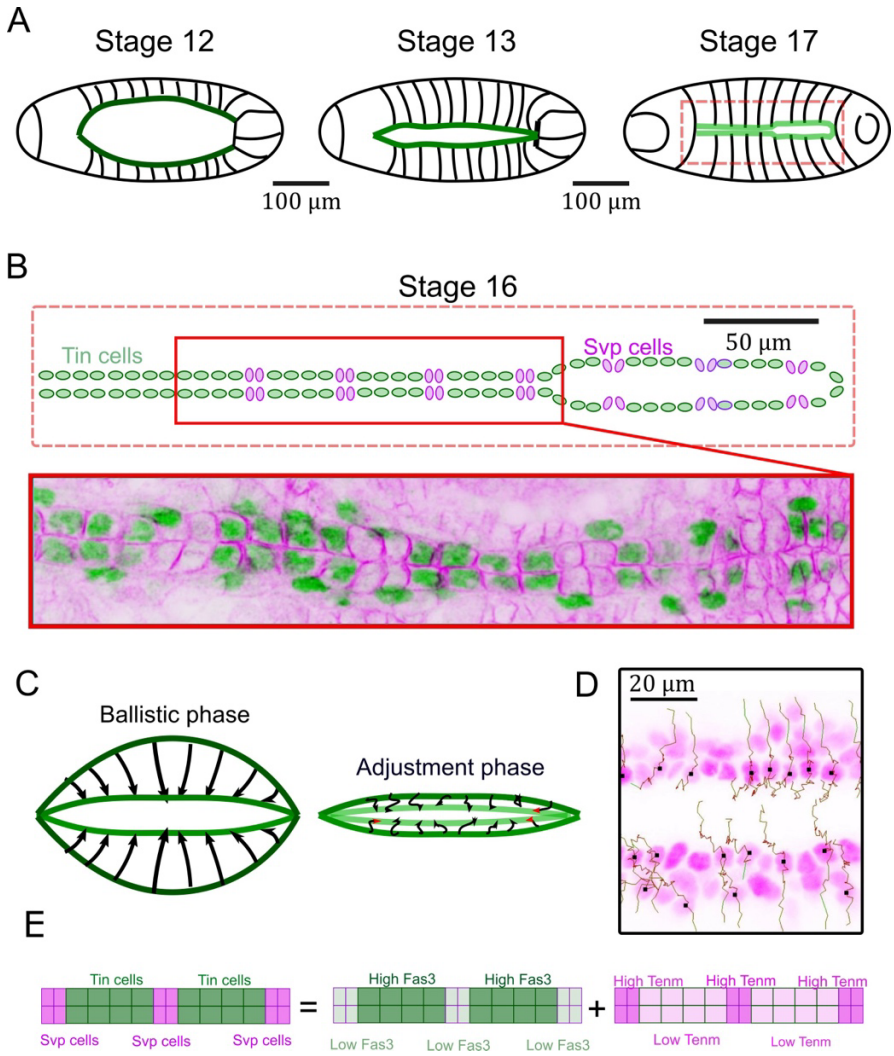

Fig. 1. Cell matching in *Drosophila* embryonic heart. (A) Developmental stages of heart formation. Cardioblasts (green regions) merge to form a tubular heart (stage 17). (B) Cardioblasts have distinct expression patterns. Heart structure at stage 16: the heart is made of a periodic alternation of Tin cells and Svp cells. Staining of cardioblasts (Spectrin in magenta and Tinman in green). (C) Heart formation is initially driven by a global tissue movement (a ballistic phase in which cardiac cells are passively driven by the dorsal closure process). Once the two contralateral rows of cardioblasts are almost in contact, active processes align cells in a final adjustment phase. (D) Example of cell trajectories during the ballistic (straight trajectories) and adjustment phase (diffusive trajectories). (E) Cardioblasts express the adhesion molecules Fas3 and Ten-m in an alternating pattern.

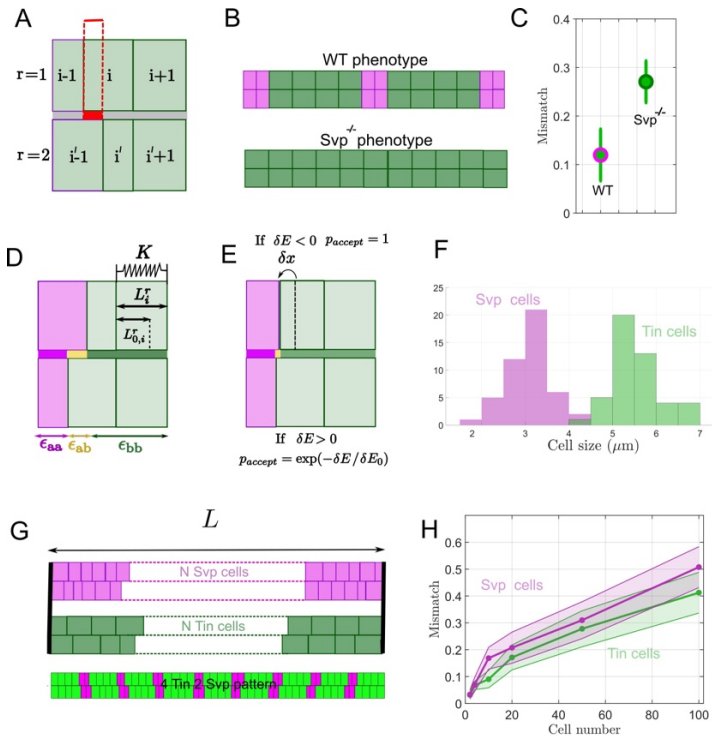

Fig. 2: Simulating heart matching (A) Definition of cell mismatch. *r=1,2* denotes two contralateral rows of cardioblasts. The dashed red box denotes a "mismatched" region in which two cells which are not supposed to be in contact are partially facing. (B) The wildtype heart (top) has a stereotypic pattern of cardioblast fates (denoted by magenta (Svp positive) and green (Tin positive) cells), which express specific adhesion molecules. Such a pattern is lost in *svp*$^{-/-}$ mutants (bottom), where there is a single cardioblast type, Tin cells. (C) It has been experimentally shown by some of us that heart cell mismatch (as defined in Fig. 2A) is affected by the loss of adhesion pattern in *svp*$^{-/-}$ mutants (41). (D) Considering two cell types (denoted by *a* (magenta) and *b* (green)) there are three interface energies: ε_{aa} between two cells of type a, ε_{bb} between two cells of type b, and ε_{ab} between cells of different type (denoted by yellow region). Cells can deform elastically (or compress), L_i from their rest length, L_0 with a compressibility K and cell-cell contact is characterized by an adhesion depending on the contact type. (E) To find how cell differential adhesion competes with the elastic deformations generated by local cell compression, a metropolis algorithm is used to find the final cell alignment after equilibration. At each step, a cell/cell interface is randomly chosen and is displaced by δx, which follows a Gaussian distribution (see Methods). The probability to accept the displacement follows the Metropolis algorithm. (F) Experimental distribution of leading-edge size in different cardioblast types (41). (G) Simulations with only one cell type (all Svp or all Tin) and with the alternating pattern of Tin/Svp cells (bottom). (H) Predicted mismatch in hearts with one cell type for different cell number. The mismatch increases with the linear size of the system (the number of cells in a heart row) as each cell width varies as a random variable.

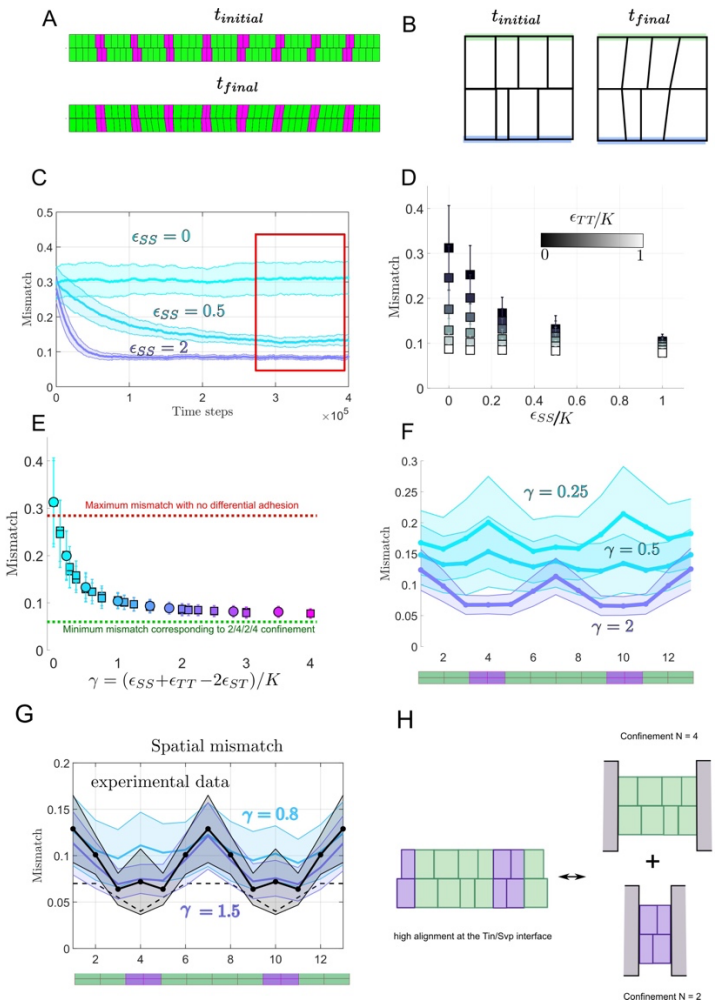

Fig. 3: The interplay between differential adhesion, cell compressibility and cell size variability determines cell-matching. (A) $t_{initial}$ corresponds to the initial configuration randomly sampled for 52 cells (4 Tin/2 Svp alternated pattern) and t_{final} corresponds to the cells configuration after convergence of mismatch. (B) Cell lengths have changed on the cell/cell interface while we still represent their initial length and position on the side not touching the interface (blue and green interfaces). (C) Ensemble averaged (N_2 = 30 simulated embryos) mismatch evolution for different values of ε_{SS} and K = 1. All mismatches are calculated at steady state. (D) Final mismatch for different values of ε_{SS} and ε_{TT}. (E) Final mismatch for different values of γ. Circles correspond to the case $\varepsilon_{ST} = 0$ and squares to $\varepsilon_{ST} \neq 0$. (F) Spatial variation of mismatch across different cell types as depicted in the below cartoon (green = Tin positive cardioblasts, magenta = Svp positive cardioblasts.). (G) Spatial variations of the mismatch in the wildtype (in black) and comparison with the simulation (blue, purple). (H) Sketch showing how differential adhesion aligns heterogeneous cell-cell contacts, which generates local confinement of cells.

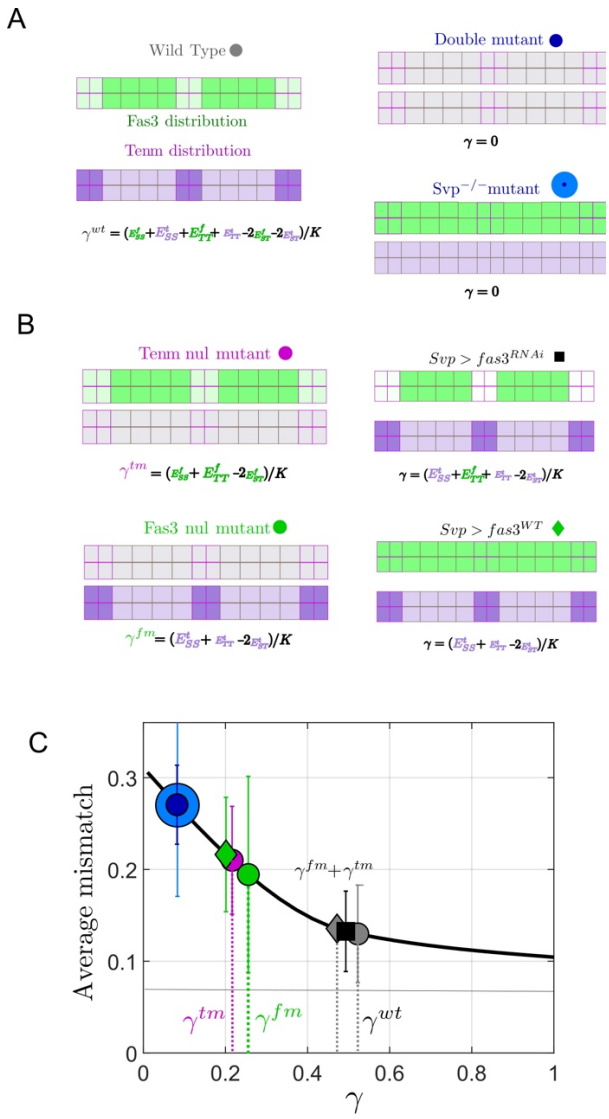

Fig. 4: Equilibrium energy description replicates experimental observations in wild type and mutants. (A) Distribution of Fas3 (green) and Ten-m (purple) in wildtype embryos and the associated formula for γ. (B) Cartoons of relative interactions in different genotypes: wildtype (grey circle); *fas3*$^{-/-}$ *ten-m*$^{-/-}$ (blue small circle); *svp*$^{-/-}$ (blue circle); *fas3*$^{-/-}$ (green circle); *ten-m*$^{-/-}$ (purple circle); Svp-Gal4, Fas3-UAS (green diamond); and Svp-Gal4 > Fas3-RNAi-UAS (black square). Each adhesion energy can be decomposed into two contributions from Tin and Svp positive cells, leading to an approximation of γ. (C) Distribution of Fas3 and Ten-m mismatch in different genotypes (as defined in (B)) overlayed on the master mismatch curve of Fig. 2E. By placing the mismatch values on the curve, we can infer the corresponding effective γ on the *x* axis, with error bars representing the estimated error.

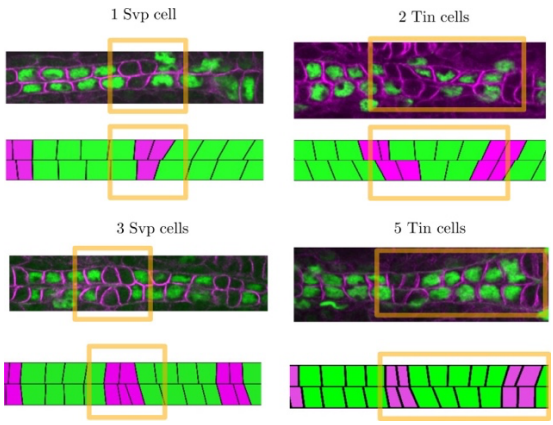

Fig. 5: Matching correction of local defects. Various types of experimentally observed cell number defects in wild type embryonic hearts. Differential adhesion can partially compensate these defects by deforming cells in the range of $\gamma \approx 0.5$ found in Fig.4.

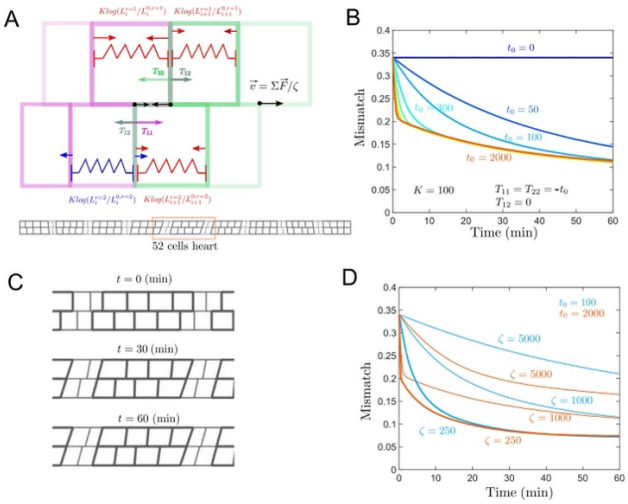

Fig. 6: Simulating cell matching dynamics (A) Vertex model implementation of interface dynamics. Each cell-cell lateral boundary on a row is defined by a vertex point. Elastic forces are represented in red/blue depending on if cells are stretched/compressed. Each cell-cell interface section between the two facing rows has a negative tension which acts on the vertices applying forces represented in magenta/green/grey depending on the interface type. The sum of these contributions divided by a friction coefficient, ξ, gives the vertex velocity. (B) We evolve the system (Methods) and compute the ensemble averaged mismatch over time (N = 30). We vary the tension t_0 between 0 and 2000 while K is fixed to 100 and $\xi = 1000$. (C) Spatial alignment for 0 min, 30 min, 60 min for $t_0 = 2000$, K= 100 and $\xi = 1000$ (D) Adhesion-independent cell alignment between cells of the same type depends on the friction coefficient ξ. Results shown for two different tensions, t_0.

554 **References**

555

556 1. Lecuit T, Le Goff L. Orchestrating size and shape during morphogenesis. Nature.
557 2007;450:189.
558 2. Heisenberg CP, Bellaiche Y. Forces in tissue morphogenesis and patterning. Cell.
559 2013;153:948.
560 3. Collinet C, Rauzi M, Lenne PF, Lecuit T. Local and tissue-scale forces drive oriented
561 junction growth during tissue extension. Nat Cell Biol. 2015;17:1247.
562 4. Pinheiro D, Bellaiche Y. Mechanical Force-Driven Adherens Junction Remodeling and
563 Epithelial Dynamics. Dev Cell. 2018;47:3.
564 5. Athilingam T, Tiwari P, Toyama Y, Saunders TE. Mechanics of epidermal
565 morphogenesis in the Drosophila pupa. Semin Cell Dev Biol. 2021;120:171.
566 6. Olivotto I, Cecchi F, Poggesi C, Yacoub MH. Developmental origins of hypertrophic
567 cardiomyopathy phenotypes: a unifying hypothesis. Nat Rev Cardiol. 2009;6:317.
568 7. Bruneau BG. The developing heart: from The Wizard of Oz to congenital heart
569 disease. Development. 2020;147:dev194233.
570 8. Som PM, Naidich TP. Illustrated review of the embryology and development of the
571 facial region, part 2: Late development of the fetal face and changes in the face from the
572 newborn to adulthood. AJNR Am J Neuroradiol. 2014;35:10.
573 9. Zhang S, Saunders T. Mechanical processes underlying precise and robust cell
574 matching. Semin Cell Dev Biol. 2021;120:75.
575 10. Dixon MJ, Marazita ML, Beaty TH, Murray JC. Cleft lip and palate: understanding
576 genetic and environmental influences. Nat Rev Genet. 2011;12:167.
577 11. Clandinin TR, Zipursky SL. Making connections in the fly visual system. Neuron.
578 2002;35:827.
579 12. Sanes JR, Yamagata M. Many paths to synaptic specificity. Annu Rev Cell Dev Biol.
580 2009;25:161.
581 13. Pinto-Teixeira F, Koo C, Rossi AM, Neriec N, Bertet C, Li X, et al. Development of
582 Concurrent Retinotopic Maps in the Fly Motion Detection Circuit. Cell. 2018;173:485.
583 14. Takeichi M. The cadherin superfamily in neuronal connections and interactions. Nat
584 Rev Neurosci. 2007;8:11.
585 15. Hong W, Mosca TJ, Luo L. Teneurins instruct synaptic partner matching in an
586 olfactory map. Nature. 2012;484:201.
587 16. Maness PF, Schachner M. Neural recognition molecules of the immunoglobulin
588 superfamily: signaling transducers of axon guidance and neuronal migration. Nature
589 Neuroscience. 2006;10:19.
590 17. Berns DS, DeNardo LA, Pederick DT, Luo L. Teneurin-3 controls topographic circuit
591 assembly in the hippocampus. Nature. 2018;554:328.
592 18. Harada T, Harada C, Parada LF. Molecular regulation of visual system development:
593 more than meets the eye. Genes Dev. 2007;21:367.
594 19. Kumar JP. Building an ommatidium one cell at a time. Dev Dyn. 2012;241:136.
595 20. Wartlick O, Julicher F, Gonzalez-Gaitan M. Growth control by a moving morphogen
596 gradient during Drosophila eye development. Development. 2014;141:1884.
597 21. Olson EN. Gene regulatory networks in the evolution and development of the heart.
598 Science. 2006;313:1922.

599 22. Hunter GL, Hadjivasiliou Z, Bonin H, He L, Perrimon N, Charras G, et al. Coordinated
600 control of Notch/Delta signalling and cell cycle progression drives lateral inhibition-
601 mediated tissue patterning. Development. 2016;143:2305.
602 23. Shaya O, Binshtok U, Hersch M, Rivkin D, Weinreb S, Amir-Zilberstein L, et al. Cell-
603 Cell Contact Area Affects Notch Signaling and Notch-Dependent Patterning. Dev Cell.
604 2017;40:505.
605 24. Schotz EM, Burdine RD, Julicher F, Steinberg MS, Heisenberg CP, Foty RA.
606 Quantitative differences in tissue surface tension influence zebrafish germ layer positioning.
607 HFSP J. 2008;2:42.
608 25. Manning ML, Foty RA, Steinberg MS, Schoetz EM. Coaction of intercellular adhesion
609 and cortical tension specifies tissue surface tension. Proc Natl Acad Sci U S A.
610 2010;107:12517.
611 26. Foty RA, Pfleger CM, Forgacs G, Steinberg MS. Surface tensions of embryonic tissues
612 predict their mutual envelopment behavior. Development. 1996;122:1611.
613 27. Foty RA, Steinberg MS. The differential adhesion hypothesis: a direct evaluation. Dev
614 Biol. 2005;278:255.
615 28. Gibson MC, Patel AB, Nagpal R, Perrimon N. The emergence of geometric order in
616 proliferating metazoan epithelia. Nature. 2006;442:1038.
617 29. Umetsu D, Aigouy B, Aliee M, Sui L, Eaton S, Julicher F, et al. Local increases in
618 mechanical tension shape compartment boundaries by biasing cell intercalations. Curr Biol.
619 2014;24:1798.
620 30. Hamant O, Heisler MG, Jonsson H, Krupinski P, Uyttewaal M, Bokov P, et al.
621 Developmental patterning by mechanical signals in Arabidopsis. science. 2008;322:1650.
622 31. Taniguchi K, Maeda R, Ando T, Okumura T, Nakazawa N, Hatori R, et al. Chirality in
623 planar cell shape contributes to left-right asymmetric epithelial morphogenesis. Science.
624 2011;333:339.
625 32. Hervieux N, Dumond M, Sapala A, Routier-Kierzkowska AL, Kierzkowski D, Roeder
626 AH, et al. A Mechanical Feedback Restricts Sepal Growth and Shape in Arabidopsis. Curr
627 Biol. 2016; 26: 1019.
628 33. Le Garrec JF, Dominguez JN, Desgrange A, Ivanovitch KD, Raphael E, Bangham JA, et
629 al. A predictive model of asymmetric morphogenesis from 3D reconstructions of mouse
630 heart looping dynamics. Elife. 2017;6:28951.
631 34. Hamant O, Saunders TE. Shaping Organs: Shared Structural Principles Across
632 Kingdoms. Annu Rev Cell Dev Biol. 2020;36:385.
633 35. Matejcic M, Salbreux G, Norden C. A non-cell-autonomous actin redistribution
634 enables isotropic retinal growth. PLoS Biol. 2018;16:e2006018.
635 36. Collier JR, Monk NA, Maini PK, Lewis JH. Pattern formation by lateral inhibition with
636 feedback: a mathematical model of delta-notch intercellular signalling. Journal of
637 theoretical Biology. 1996;183:429.
638 37. Bi D, Lopez JH, Schwarz JM, Manning ML. A density-independent rigidity transition in
639 biological tissues. Nature Physics. 2015;11:1074.
640 38. Kim S, Cassidy JJ, Yang B, Carthew RW, Hilgenfeldt S. Hexagonal Patterning of the
641 Insect Compound Eye: Facet Area Variation, Defects, and Disorder. Biophys J.
642 2016;111:2735.
643 39. Lou Y, Rupprecht JF, Theis S, Hiraiwa T, Saunders TE. Curvature-Induced Cell
644 Rearrangements in Biological Tissues. Phys Rev Lett. 2023;130:108401.

40. Hayashi T, Carthew RW. Surface mechanics mediate pattern formation in the developing retina. Nature. 2004;431:647.
41. Zhang S, Amourda C, Garfield D, Saunders TE. Selective Filopodia Adhesion Ensures Robust Cell Matching in the Drosophila Heart. Dev Cell. 2018;46:189.
42. Zhang S, Teng X, Toyama Y, Saunders TE. Periodic Oscillations of Myosin-II Mechanically Proofread Cell-Cell Connections to Ensure Robust Formation of the Cardiac Vessel. Curr Biol. 2020;30:3364.
43. Zhang S, Saunders TE. Protocol for batch imaging and quantification of cellular mismatch during Drosophila embryonic heart formation. STAR Protoc. 2021;2:100817.
44. Bodmer R, Frasch M. Development and aging of the Drosophila heart. Heart Development and Regeneration: Elsevier; 2010. p. 47-86.
45. Haack T, Schneider M, Schwendele B, Renault AD. Drosophila heart cell movement to the midline occurs through both cell autonomous migration and dorsal closure. Dev Biol. 2014;396:169.
46. Balaghi N, Erdemci-Tandogan G, McFaul C, Fernandez-Gonzalez R. Myosin waves and a mechanical asymmetry guide the oscillatory migration of Drosophila cardiac progenitors. Developmental Cell. 2023;58:1299.
47. Krauth W. Statistical mechanics: algorithms and computations: OUP Oxford; 2006.
48. Metropolis N, Rosenbluth AW, Rosenbluth MN, Teller AH, Teller E. Equation of State Calculations by Fast Computing Machines. The Journal of Chemical Physics. 1953;21:1087.
49. Kuntz SG, Eisen MB. Drosophila embryogenesis scales uniformly across temperature in developmentally diverse species. PLoS genetics. 2014;10:e1004293.
50. Chong J, Amourda C, Saunders TE. Temporal development of Drosophila embryos is highly robust across a wide temperature range. J R Soc Interface. 2018;15:20180304.
51. Tiwari P, Rengarajan H, Saunders TE. Scaling of internal organs during Drosophila embryonic development. Biophysical Journal. 2021;120:4264.
52. Atia L, Bi D, Sharma Y, Mitchel JA, Gweon B, Koehler S, et al. Geometric constraints during epithelial jamming. Nat Phys. 2018;14:613.
53. Atia L, Fredberg JJ, Gov NS, Pegoraro AF. Are cell jamming and unjamming essential in tissue development? Cells Dev. 2021;168:203727.
54. Yang S, Palmquist KH, Nathan L, Pfeifer CR, Schultheiss PJ, Sharma A, et al. Morphogens enable interacting supracellular phases that generate organ architecture. Science. 2023;382:eadg5579.
55. Bentley K, Mariggi G, Gerhardt H, Bates PA. Tipping the balance: robustness of tip cell selection, migration and fusion in angiogenesis. PLoS Comput Biol. 2009;5:e1000549.
56. Sonnemann KJ, Bement WM. Wound repair: toward understanding and integration of single-cell and multicellular wound responses. Annu Rev Cell Dev Biol. 2011;27:237.
57. Koser DE, Thompson AJ, Foster SK, Dwivedy A, Pillai EK, Sheridan GK, et al. Mechanosensing is critical for axon growth in the developing brain. Nat Neurosci. 2016;19(12):1592.
58. Barriga EH, Franze K, Charras G, Mayor R. Tissue stiffening coordinates morphogenesis by triggering collective cell migration in vivo. Nature. 2018;554:523.